JOURNAL OF UNDERGRADUATE RESEARCH

The Importance of Tissue Identity in Modeling Transcranial Direct Current Stimulation

Giovana Silva, Tyler Busch, Samantha Pedersen, Kevin Iversen, Priya Sambasivan, Ruogu Fang, Adam Woods, & Aprinda Indahlastari Queen

College of Public Health and Health Professions, University of Florida

Mentor: Aprinda Indahlastari Queen, Department of Clinical and Health Psychology

Abstract

Transcranial direct current stimulation (tDCS) is a non-invasive brain stimulation technique that uses scalp electrodes to deliver electrical currents, altering neuronal activity. Research suggests that tDCS can enhance cognitive functions (e.g., working memory) in older adults by modulating brain activity, but outcomes have varied due to inter-individual anatomical differences. This study investigates how head tissue segmentation affects delivered current density (J) in the brain. Six models (M1–M6) were created from T1-weighed MRIs of four older adults (2M, 2F, M_{age} = 73 years). The reference model (M6) included the six commonly used tissue types: white matter, grey matter, CSF, skin, and bone. Models M2–M5 each added one additional tissue type (blood, eye, fat, and the separation of bone into cancellous and cortical bone) to assess their effects on current density. Model M1 included all eleven tissue types. Conductivity values were assigned using literature-derived data. Electric fields were simulated in COMSOL Multiphysics®, and brain current density (Jbrain) was calculated by combining the resulting white and gray matter. Electrodes were placed at the F3 (cathode) - F4 (anode) montage with a 2mA input current. Jbrain values in models M1-M5 were compared to M6 using Welch's t-tests in RStudio. Results showed significant differences in models M1 (median Jbrain = 0.020381 Am^{-2}), M4 (median Jbrain = 0.018377 Am^{-2}), and M5 (median Jbrain = 0.015608 Am^{-2}) compared to the reference model, M6 (p-value <0.001). This study highlights the importance of segmenting fat, cortical, and cancellous bone on resulting current density in the brain, as well as considering individual variability to model tDCS in aging populations.

Introduction

Transcranial direct current stimulation (tDCS) is a non-invasive technique that introduces weak electrical currents (2-4mA) to the brain to modulate neuronal membrane potentials (Indahlastari, Hardcastle, et al., 2021). Changes in the synaptic environment facilitate inhibitory or excitatory responses and create a phenotypic effect on an individual's behavior (Thair et al., 2017). The therapy has been found to assist in relieving chronic pain and restoring post-stroke motor and speech functions (Ho et al., 2022), among others. A systematic review and metaanalysis found thirteen studies that showed that tDCS can improve cognition in older adults without cognitive impairments (Indahlastari et al., 2021), known as cognitively healthy individuals. Age-related cognitive changes are a normal part of healthy aging and can be evaluated by assessing cognitive abilities, such as working memory (the capacity to temporarily hold and manipulate information) before and after tDCS administration (Christensen, 2001).

Despite its potential effectiveness, individual therapeutic results on the efficacy of tDCS for improving cognitive and behavioral outcomes remain inconsistent (Vergallito et al., 2022). This variability is largely attributed to anatomical variations in tissues, including differences in the volumes of cerebrospinal fluid (CSF) and brain matter, which can affect electrical current distribution in the brain (Vergallito et al., 2022). Developing finite element method (FEM) models based on Magnetic Resonance Imaging (MRI) can predict current pathways, allowing for personalized adjustments to stimulation parameters. The FEM pipeline used for creating tDCS models includes a segmentation process where different head tissue types are identified and labeled according to their anatomical locations. This step is essential for understanding how different types of tissue (e.g., bone, soft tissue, etc.) influence the modification of electrical pathways. After segmentation, each tissue type is assigned a corresponding conductivity value, defining its capacity to conduct an electrical current. The segmented head tissues are input into the FEM pipeline to obtain current density (J) as a measure of the amount of delivered current resulting from tDCS application (Albizu et al., 2020).

Historically, the standard MRI-derived tDCS automatic modeling pipeline involves dividing the head into six tissues (gray matter, white matter, CSF, skull, scalp, and air) (Huang et al., 2012; Huang, Datta & Parra 2020). There is increased interest in expanding model complexity to include up to fifteen tissue types, including tissues such as internal air, arteries, muscles, mucous tissue, visual nerve, skin, spinal cord, veins, cortical bone, and cancellous bone (Puonti et al., 2020). Despite experimental validation of both methods, no direct comparison has been made to evaluate the impact of individual tissue types on electric fields. This research aims to address this gap by examining the effects of various tissue identities on tDCS models.

To explore the contribution of each tissue type, six different models were constructed, each isolating specific tissues based on previous research. The first model, which includes the greatest number of tissues, aims to segment T1-weighted MRI scans across a broad range of tissue types to enhance the precision of electric field predictions. Subsequent models focus on isolating blood vessels, eyes, fat tissue, and cancellous and cortical bone. The final model serves as the reference, segmenting the head into the six tissue types historically used in the field. This study seeks to determine whether models produce different electrical field distributions compared to the standard six-tissue model, and whether they are equally effective in predicting current pathways through the brain (Jbrain) during stimulation.

Methods

Four older adults without cognitive impairments (2M, 2F, M_{age} = 73 years), defined by MoCA scores above 25, were selected from the Augmenting Cognitive Training in Older Adults (ACT) database (Woods et al., 2018) for this pilot study to balance feasibility with capturing inter-individual anatomical variability. The database provided T1-weighted MRI scans segmented into 11 tissue types using Synopsys' Simpleware™ ScanIP. Each participant was segmented into six different models (see Table 1), isolating individual tissues for significance, resulting in a total of 24 samples. Tissue conductivities (σ in S/m) were assigned as follows: WM (0.126), GM (0.276), CSF (1.65), bone (0.01), cortical bone (0.008), cancellous bone (0.02), skin (0.465), fat (0.025), blood (0.6), eyes (0.5), and muscle (0.16), consistent with prior studies (Indahlastari, Albizu, et al., 2021).

Table 1. Identification of the six models studied and their tissue division. Models were determined based on existent tissue segmentation and newly proposed models to determine the relevance of specific tissues to the current density (J) value of the brain.

Model Name	Tissue Types
M1 (Derived)	White matter, grey matter, skin, fat, muscle, air, CSF, cancellous bone, cortical bone, blood vessels, eyes (11)
M2 (Derived)	White matter, grey matter, soft tissue, CSF, air, bone, **blood vessels** (7)
M3 (Derived)	White matter, grey matter, soft tissue, CSF, air, bone, **eyes** (7)
M4 (Derived)	White matter, grey matter, soft tissue, CSF, air, bone, **fat** (7)
M5 (Derived)	White matter, grey matter, soft tissue, CSF, air, **cancellous bone, cortical bone** (7)
M6 (Reference)	White matter, grey matter, CSF, bone, air, soft tissue (6)

Model Construction

All models were derived from T1-weighted MRIs acquired with a 3 Tesla scanner and preprocessed using FreeSurfer (Stolte et al., 2024). Each MRI is segmented into the six models as described below and seen in Table 1. Each model included specific tissues to evaluate their contribution to whole-brain current density (Jbrain). Final segmented tissues were individually checked for overlaps, binarized, and exported for subsequent use.

model 1 (M1).

M1 segmentation followed Stolte et al. (2024), where segmentation for white matter (including spinal cord and optic nerves), gray matter, air, and bone were manually corrected from the automatic segmentation output. Blood vessels, skin, fat, eyes, CSF, muscle tissues, and air were manually segmented. Blood vessels were limited to the arterial tissues from the neck to the brain.

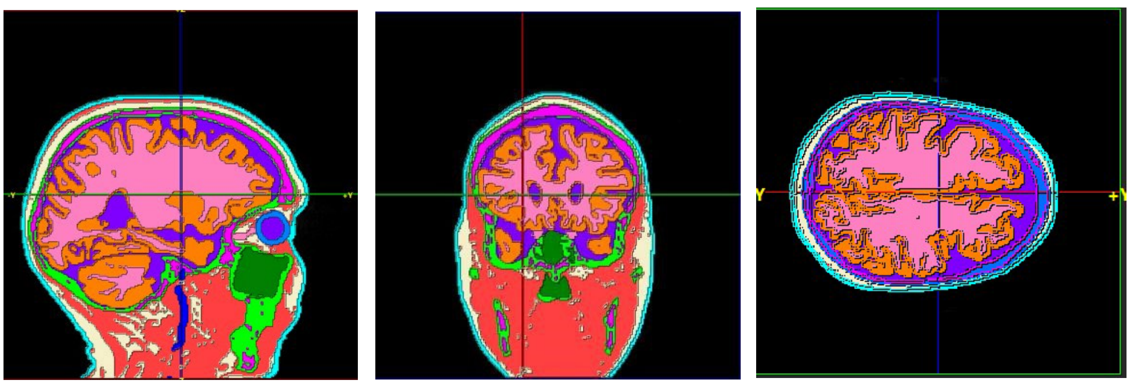

Figure 1. Model 1 (M1) of 11 tissues in sagittal, coronal, and transverse planes (left to right). *Note*. M1 is composed of white matter (pink), grey matter (orange), skin (light blue), fat (white), muscle (red), air (dark green), CSF (purple), cancellous bone (magenta), cortical bone (light green), blood vessels (navy), and eyes (dark blue).

model 2 (M2).

Using the final, quality-checked version of M1, M2 was generated by importing the white matter, grey matter, fat, skin, CSF, muscle, air, eyes, and blood vessels, as well as the participant's T1-weighted image, into Simpleware™. The bone mask without the separation of cancellous and cortical tissue in M1 was also imported. Boolean subtractions were performed between preprocessed bone, air, and white matter, and between bone and blood vessels to eliminate overlap between the masks. After subtraction, Boolean unions were created between the eyes and CSF to form the "CSF" mask to follow the standard in the field (Huang, Datta & Parra 2020). The Boolean operation was also used to combine skin, fat, and muscle to create the "soft tissue" mask.

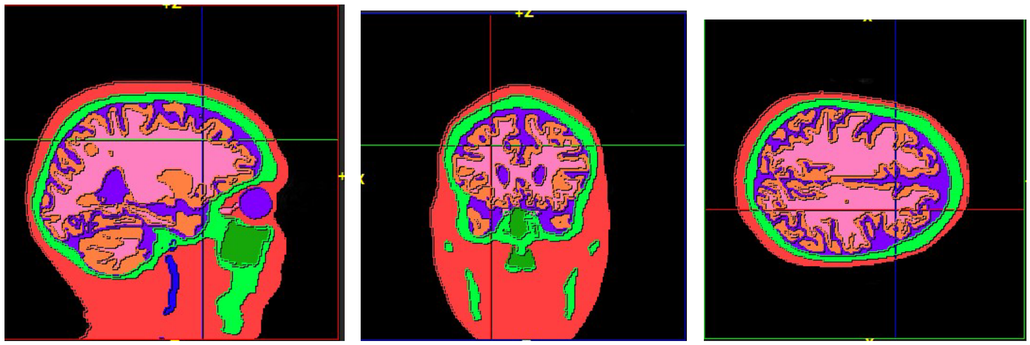

Figure 2. Model 2 (M2) of seven tissues in sagittal, coronal, and transverse planes (left to right). *Note.* M2 is composed of white matter (pink), grey matter (orange), soft tissue (red), CSF (purple), air (dark green), bone (light green), and blood vessels (navy).

model 3 (M3).

M3 imported the binarized white matter, grey matter, soft tissue, and air masks from M2, along with the CSF, eyes, and bone from M1. Empty voxels in the CSF and soft tissue masks, where blood vessels were located, were manually filled according to their neighboring tissue identity. The bone mask was used as a boundary between CSF and soft tissue masks.

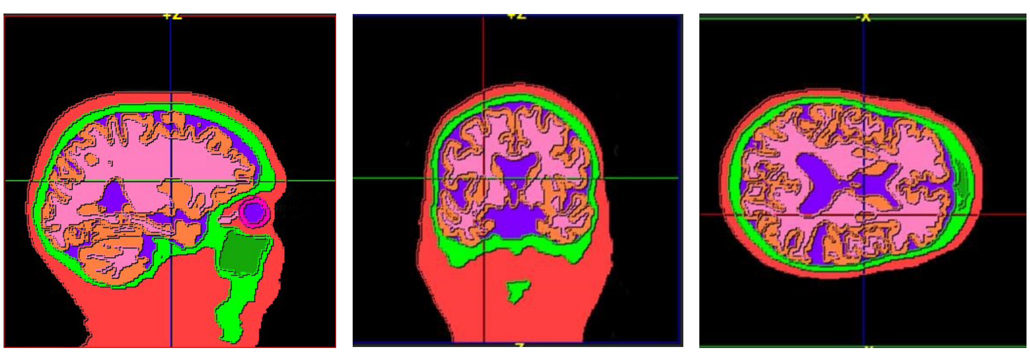

Figure 3. Model 3 (M3) of seven tissues in sagittal, coronal, and transverse planes (left to right). *Note.* M3 is composed of white matter (light pink), grey matter (orange), soft tissue (red), CSF (purple), air (dark green), bone (light green), and eyes (magenta).

model 4 (M4).

M4 was created by importing white matter, grey matter, soft tissue, air, bone, CSF, and eye masks from M3, and fat from M1. A Boolean subtraction was performed between fat and soft tissue, and a Boolean union was made between CSF and eyes.

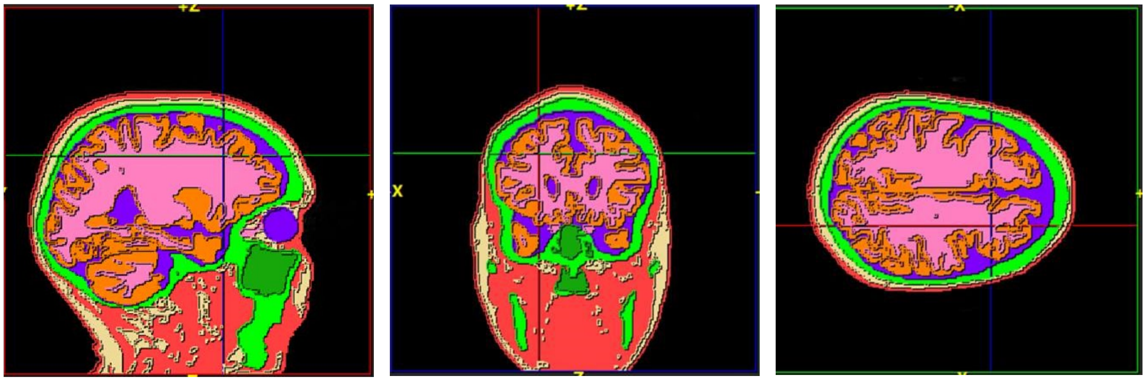

Figure 4. Model 4 (M4) of seven-tissues in sagittal, coronal, and transverse planes. *Note.* M4 is composed of white matter (pink), grey matter (orange), soft tissue (muscle and skin) (red), CSF (purple), bone (light green), air (dark green), and fat (white).

model 5 (M5).

M5 was generated by importing white matter, grey matter, CSF, and air masks from M4, soft tissue from M3, and cancellous and cortical bone from M1. Empty voxels representing blood vessels were manually filled based on neighboring voxels, including soft tissue, bone, and CSF.

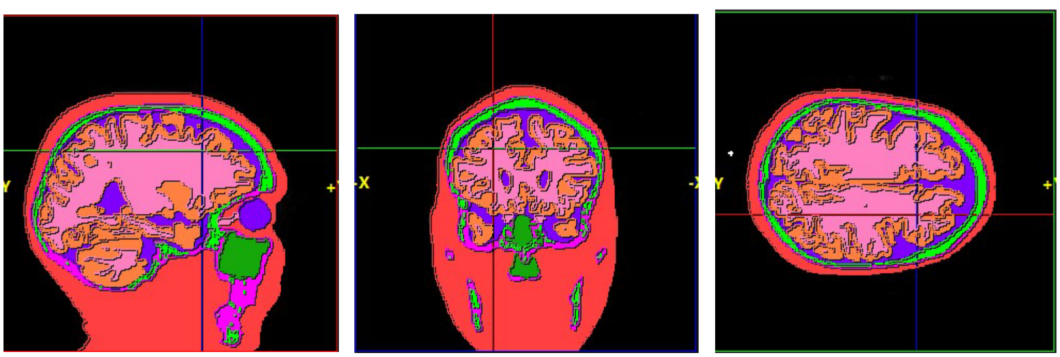

Figure 5. Model 5 (M5) of seven tissues in sagittal, coronal, and transverse planes (left to right). *Note.* M5 is composed of white matter (pink), grey matter (orange), soft tissue (red), CSF (purple), air (dark green), cortical bone (magenta), and cancellous bone (light green).

model 6 (M6).

Lastly, M6 was created by importing white matter, grey matter, CSF, air, and soft tissue masks from M5, and bone from M4. M6 served as the reference model, containing the tissue identities most used in the field.

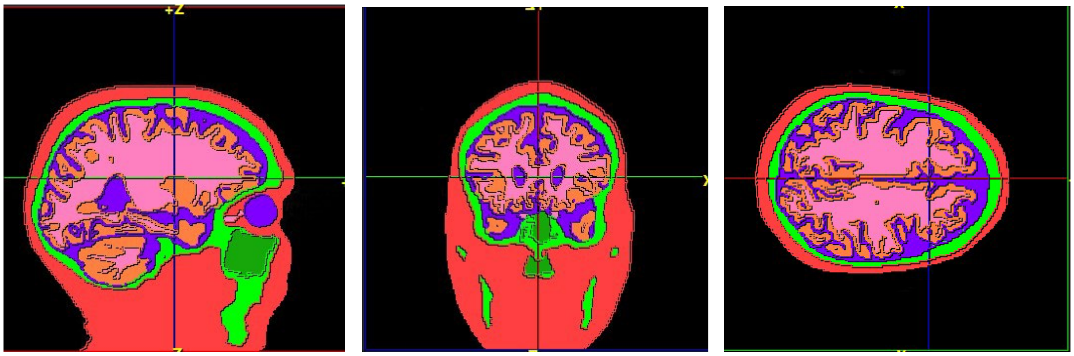

Figure 6. Model 6 (M6) of six tissues in sagittal, coronal, and transverse planes (left to right). *Note.* M6 is composed of white matter (pink), grey matter (orange), soft tissue (red), CSF (purple), air (dark green), and bone (light green).

Volume Meshing and Solution Generation

After segmentation, electrode pads and gel masks were added to the models using Simpleware™. Electrodes were generated with ROAST and manually corrected in Simpleware™ to eliminate gaps between the scalp and electrodes. Volume meshing was then generated in Simpleware™, and model physics was simulated in COMSOL Multiphysics® v.5.4 using the AC/DC module (2024). In COMSOL®, boundary conditions were set with the F3 electrode (cathode) at -2 mA and the F4 electrode (anode) at +2 mA, ensuring no current leakage on the surface of the head. The resulting model satisfied the Laplace equation, as seen in Figure 7 (Indahlastari et al., 2016). Current density results were modified to represent the vector's magnitude, defined as 'Jnorm,' and extracted to MATLAB (The MathWorks, Inc., 2024). Then, the white matter and grey matter tissues were combined as 'brain' and multiplied by J to create 'Jbrain'.

$$\nabla \cdot (\sigma \nabla \phi) = 0$$

Figure 7. The Laplace Equation.

Statistical Analysis

An independent-sample Welch's t-test was conducted using RStudio to determine if there were statistically significant differences between the M6 model and each of the derived models. A scatterplot was created to visually inspect Jbrain values.

Results

Current Density Distribution

Generated Jbrain data was visualized in MRICroGL to illustrate the current density distribution. As shown in Figures 8 and 9, there is a larger accumulation of electrical current in the frontal lobe for models M1 and M4 compared to M6 across all four participants, in both axial view and 3D rendering. A visible decrease in Jbrain is also observed in M5, indicated by the smaller, red-colored area in comparison to M6. Models M1, M2, and M5 yielded different median values when compared to M6, while M3 and M4 had similar median values. Log_{10} Jbrain values for each model, shown in Figure 10, showed a normal distribution. M1, M4, and M5 had differing results when compared to M6 (reference model) distribution, whereas M2 and M3 were similar to the reference (M6).

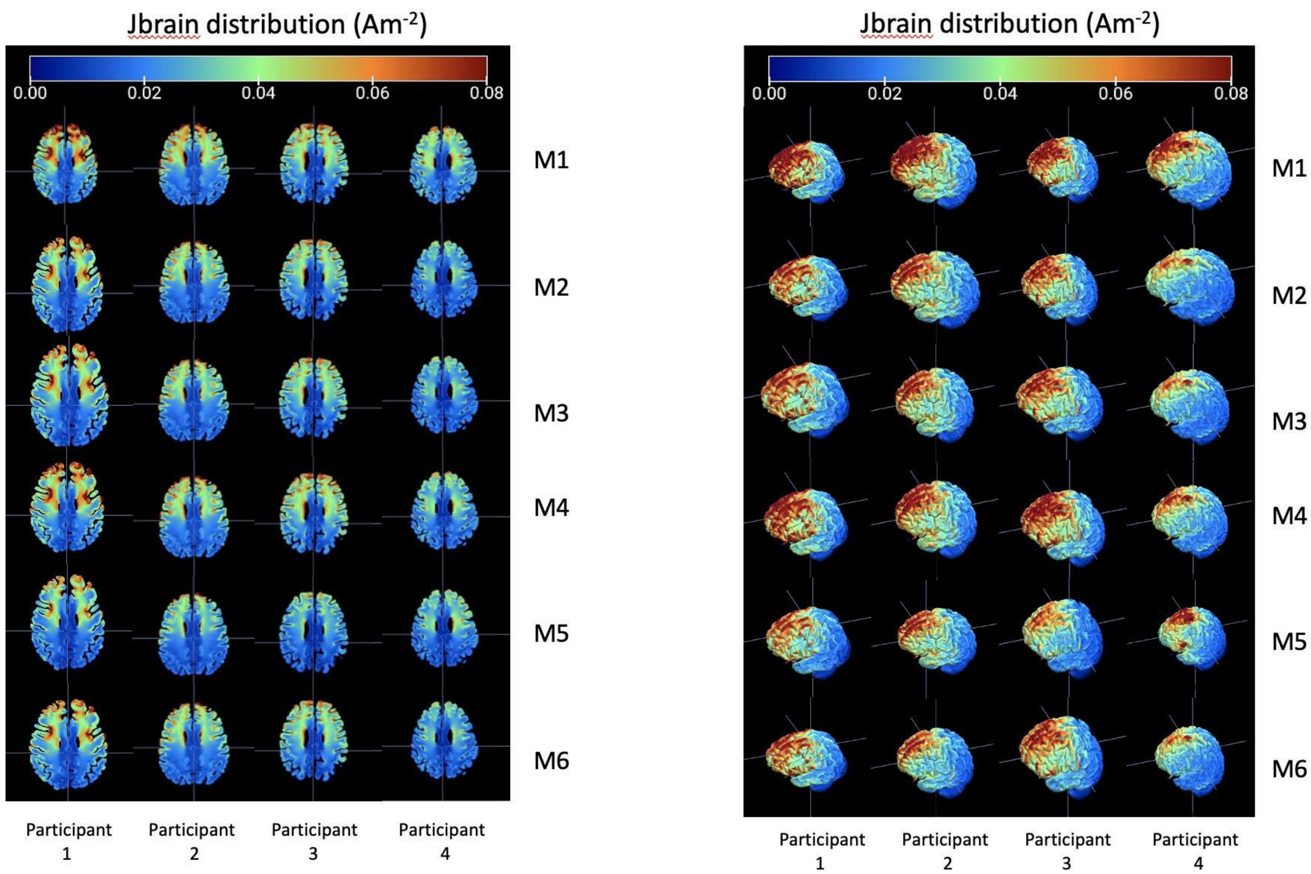

Figure 8. Visual representation of current density (J) values in all models and all participants, shown in axial view (left) and 3D rendering (right).

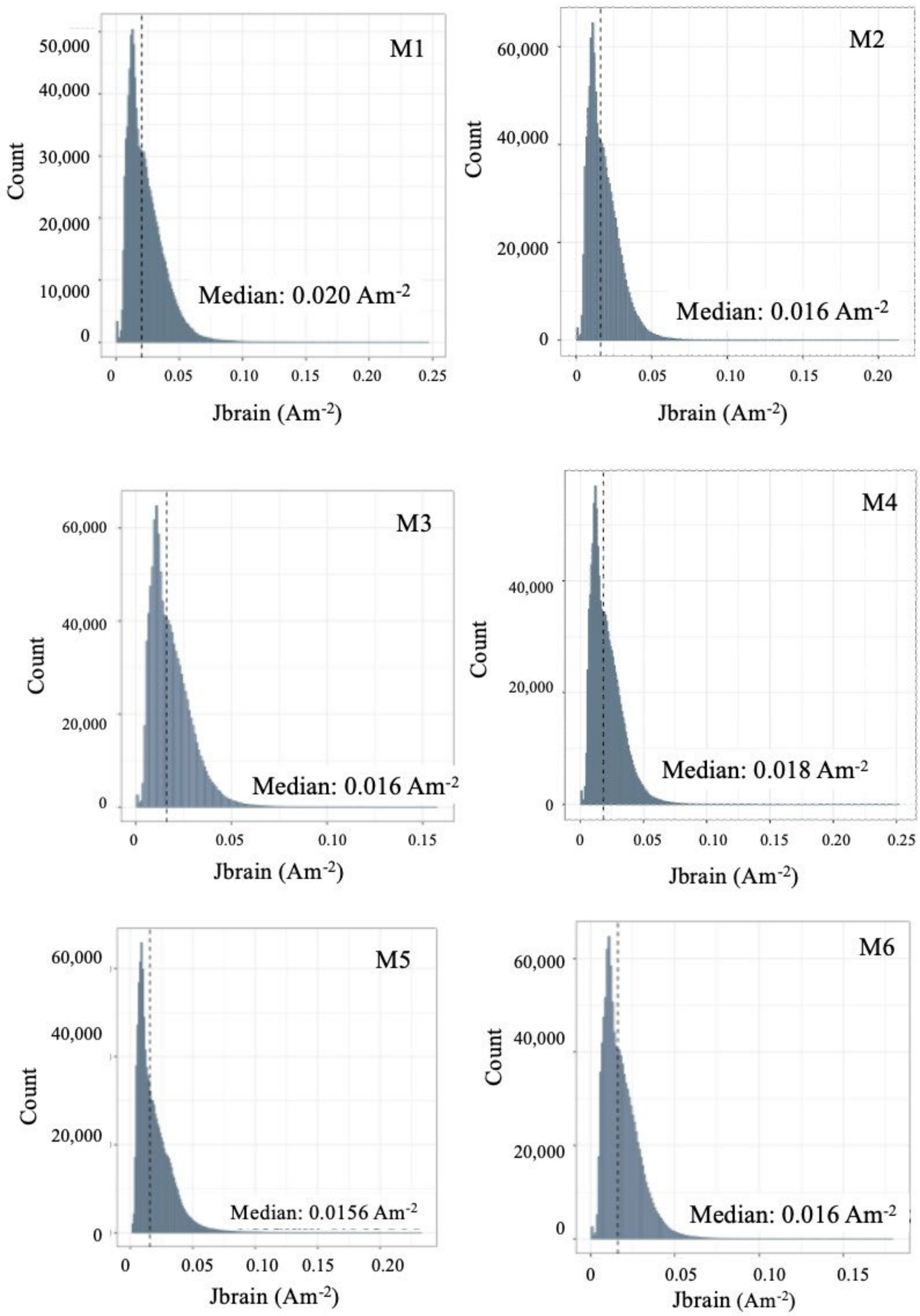

Figure 9. Current density in the brain (Jbrain) values for all models.

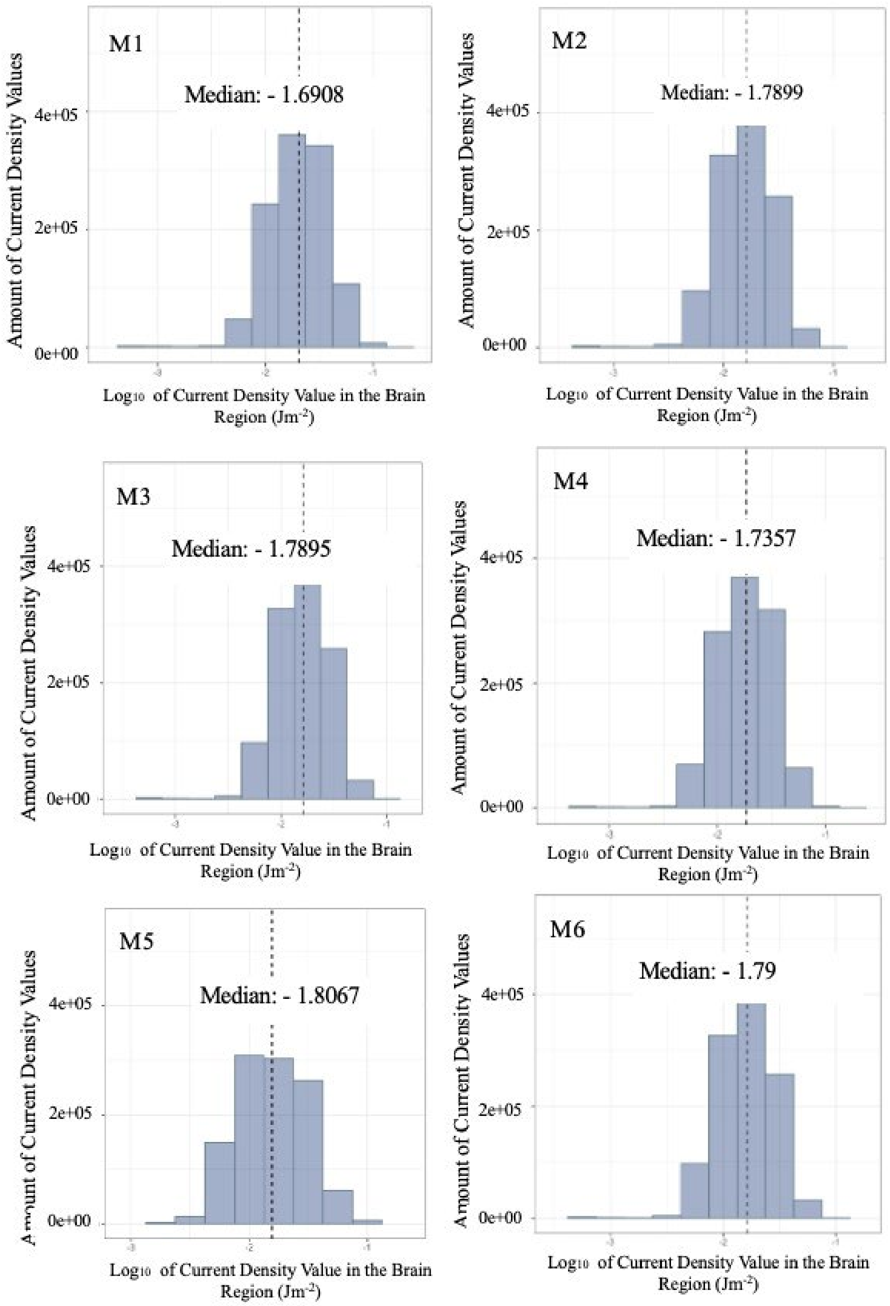

Figure 10. Logarithmically transformed (Log_{10}) current density in the brain (Jbrain) values for all models.

Statistical Analysis

A Welch's t-test, presented in Table 2, confirmed that models M1, M4, and M5 yielded statistically significant differences in J values compared to M6 ($p < 0.05$). In contrast, M2 and

M3 did not show significant differences from M6. Results varied among participants within each model, as indicated by the means reported in Table 2.

Table 2. Differences between the derived (M1-M5) models and the reference (M6) model in mean, standard deviation, and statistical significance of current density of the brain (Jbrain).

Model	Participant 1 (*M, SD, p*)	Participant 2 (*M, SD, p*)	Participant 3 (*M, SD, p*)	Participant 4 (*M, SD, p*)
M1	-1.7, 0.26, p<0.01	-1.65, 0.29, p<0.01	-1.7, 0.3, p<0.01	-1.64, 0.3, p<0.01
M2	-1.8, 0.25, p=0.9	-1.7, 0.28, p=0.42	-1.73, 0.3, p=0.21	-1.69, 0.29, p=0.8
M3	-1.8, 0.25, p=0.33	-1.7, 0.28, p=0.46	-1.73, 0.3, p=0.21	-1.69, 0.29, p=0.14
M4	-1.75, 0.26, p<0.01	-1.67, 0.28, p<0.01	-1.69, 0.3, p<0.01	-1.65, 0.30, p<0.01
M5	-1.81,0.29, p<0.01	-1.75, 0.28, p<0.01	-1.81, 0.29, p<0.01	-1.75, 0.29, p<0.01

Discussion

This study investigated the effects of various tissues (blood vessels, fat, eyes, and cancellous and cortical bone) on electric field models following tDCS. Results highlight the unique importance of segmenting fat and cancellous/cortical bone to produced current density in white and gray matter. Additionally, the findings underscore the significance of thorough tissue-specific segmentation of the tissue types included in M1 (white matter, grey matter, skin, fat, muscle, air, CSF, cancellous bone, cortical bone, blood vessels, and eyes) when analyzing current density in the brain.

Our results demonstrate that incorporating tissue-specific segmentation for fat (M4) and cortical/cancellous bone (M5) significantly alters current density predictions in tDCS models. The reduced current density in M4 aligns with previous findings by Shahid, Wen, and Ahfock (2011), who identified fat's low conductivity as a key insulator that diverts current away from superficial pathways. From the clinical perspective, age-related increases in subcutaneous fat may amplify shielding effects, potentially leading to underestimating current requirements in simplified models. Similarly, the reduction in frontal Jbrain observed in M5 reflects both conductivity contrasts and anatomical aging, as the ratio between cancellous and cortical bone changes with age. Cancellous bone is more conductive than cortical bone due to its pores filled with fluid-like substances (e.g., bone marrow) (Opitz et al., 2015). Yet, cortical bone volume may decrease with age (Blinkouskaya et al., 2015), explaining why homogenized "bone" masks (as in M6) might misrepresent current delivery in older adults due to the lack of separation between cancellous and cortical bone. These findings extend prior work by demonstrating how age-dependent tissue changes exacerbate model inaccuracies, underscoring the necessity of bone subtype segmentation to accurately estimate Jbrain doses. Together, these results advocate for anatomically detailed models in aging research, where omitting fat or conflating bone types may compromise predicted current density and contribute to inaccurate estimations of stimulation responses.

Our findings suggest that the inclusion of blood vessels in tDCS models may have a limited impact on global current density for the F3-F4 montage, contrasting with prior reports that electric fields can increase to 200V/m across the blood-brain barrier (Khadka et al., 2023). While Khadka et al. (2023) proposed that neglecting blood vessels could distort field pathways due to their high conductivity, models M2 and M3 showed no significant differences in Jbrain compared to the reference model (M6). This discrepancy may arise from the F3-F4 montage's frontal targeting, where current pathways are dominated by proximal, high-volume tissues (e.g., skin, fat, bone) rather than smaller, distal structures like blood vessels. Consistent with Miranda et al. (2006), our results emphasize that current density decreased with increased electrode distance, with tissues closer to F3/F4 (e.g., scalp, skull) disproportionately shaping Jbrain whereas remote, low-volume tissues (e.g., blood vessels, eyes) exert minimal influence despite their conductivity contrasts. This underscores the importance of considering montage-specific modeling in relation to tissue location. Therefore, these findings refine modeling best practices by suggesting for a nuanced approach where the importance of tissue inclusion is contributed by both anatomical relevance to the target brain region and proximity to the electrode sites.

Overall, our results revealed substantial inter-individual variability in current density values, underscoring the limitations of one-size-fits-all models in aging populations where anatomical heterogeneity is pronounced. To mitigate this variability, our findings advocate for individualized head models that capture critical age-related structural differences that include cancellous/cortical bone ratios and fat-muscle composition to accurately estimate tDCS delivery in older adults. Refining individualized head models will improve estimates of stimulation delivery, allowing for more effective modulation of targeted brain regions. This will allow researchers to better link current distribution to behavioral outcomes, thereby maximizing the therapeutic benefits of tDCS for improving cognition in older adults.

Limitations and Future Directions

While this study provided valuable insight into the influence of tissue inclusion to predict current density, we recognize the presence of limitations in this study. First, the sample size of four individuals may not adequately represent the diversity of head tissue anatomy among the broader aging population. Inter-individual differences in brain size and volume can alter current pathways by modulating tissue changes. Similarly, this study was limited to MRI scans from a healthy aging population. Therefore, caution is needed when generalizing these results to other populations, such as young individuals. For instance, cortical volume decreases with age (Lee & Kim, 2022), which may allow tissues other than white and gray matter to exert a greater influence on the current pathway. Furthermore, this study employed only one electrode montage (F3-F4). Exploring different electrode montages could further elucidate the relationship between tissue location and relative significance to current density and the applied electrical current.

Conclusion

Lastly, sex differences were not examined, although they might contribute to variations in median and p-values observed, as well as morphological and anatomical discrepancies between participants. Future studies should explore how linking modeled predictions with behavioral outcomes can further inform the application of tDCS in cognition and beyond.

References

AC/DC Module User's Guide, pp. 75-84. COMSOL Multiphysics® v. 5.4. COMSOL AB, Stockholm, Sweden. 2024

Albizu, A., Fang, R., Indahlastari, A., O'Shea, A., Stolte, S. E., See, K. B., Boutzoukas, E. M., Kraft, J. N., Nissim, N. R., & Woods, A. J. (2020). Machine learning and individual variability in electric field characteristics predict tDCS treatment response. *Brain Stimulation*, *13*(6), 1753–1764. https://doi.org/10.1016/j.brs.2020.10.001

Blinkouskaya, Y., Caçoilo, A., Gollamudi, T., Jalalian, S., & Weickenmeier, J. (2021). Brain aging mechanisms with mechanical manifestations. *Mechanisms of Ageing and Development, 200*, 111575. https://doi.org/10.1016/j.mad.2021.111575

Christensen, H. (2001). What Cognitive Changes Can Be Expected with Normal Ageing? *Australian & New Zealand Journal of Psychiatry, 35*(6), 768–775. https://doi.org/10.1046/j.1440-1614.2001.00966.x

Evans, C., Johnstone, A., Zich, C., Lee, J. S. A., Ward, N. S., & Bestmann, S. (2023). The impact of brain lesions on tDCS-induced electric fields. *Scientific Reports, 13*(1), 19430. https://doi.org/10.1038/s41598-023-45905-7

Ho, J. S., Slawka, E., Pacheco-Barrios, K., Cardenas-Rojas, A., Castelo-Branco, L., & Fregni, F. (2022). The pros and cons of tDCS as a therapeutic tool in the rehabilitation of chronic pain. *Principles and practice of clinical research, 8*(2), 26–30. https://doi.org/10.21801/ppcrj.2022.82.4

Huang, Y., Datta, A., & Parra, L. C. (2020). Optimization of interferential stimulation of the human brain with electrode arrays. *Journal of Neural Engineering, 17*(3), 036023. https://doi.org/10.1088/1741-2552/ab92b3

Huang, Y., Su, Y., Rorden, C., Dmochowski, J., Datta, A., & Parra, L. C. (2012). An automated method for high-definition transcranial direct current stimulation modeling. *Annual International Conference of the IEEE Engineering in Medicine and Biology Society. IEEE Engineering in Medicine and Biology Society. Annual International Conference*, *2012*, 5376–5379. https://doi.org/10.1109/EMBC.2012.6347209

Indahlastari, A., Albizu, A., Kraft, J. N., O'Shea, A., Nissim, N. R., Dunn, A. L., Carballo, D., Gordon, M. P., Taank, S., Kahn, A. T., Hernandez, C., Zucker, W. M., & Woods, A. J. (2021). Individualized tDCS modeling predicts functional connectivity changes within the working memory network in older adults. *Brain Stimulation, 14*(5), 1205–1215. https://doi.org/10.1016/j.brs.2021.08.003

Indahlastari, A., Albizu, A., O'Shea, A., Forbes, M. A., Nissim, N. R., Kraft, J. N., Evangelista, N. D., Hausman, H. K., & Woods, A. J. (2020). Modeling transcranial electrical stimulation in the aging brain. *Brain Stimulation, 13*(3), 664–674.https://doi.org/10.1016/j.brs.2020.02.007

Indahlastari, A., Chauhan, M., Schwartz, B., & Sadleir, R. J. (2016). Changing head model extent affects finite element predictions of transcranial direct current stimulation distributions. *Journal of Neural Engineering, 13*(6), 066006. https://doi.org/10.1088/1741-2560/13/6/066006

Indahlastari, A., Hardcastle, C., Albizu, A., Alvarez-Alvarado, S., Boutzoukas, E. M., Evangelista, N. D., Hausman, H. K., Kraft, J., Langer, K., & Woods, A. J. (2021). A Systematic Review and MetaAnalysis of Transcranial Direct Current Stimulation to Remediate Age-Related Cognitive Decline in Healthy Older Adults. *Neuropsychiatric Disease and Treatment, 17*, 971–990. https://doi.org/10.2147/NDT.S259499

Khadka, N., Poon, C., Cancel, L. M., Tarbell, J. M., & Bikson, M. (2023). Multi-scale multi-physics model of brain interstitial water flux by transcranial Direct Current Stimulation. *Journal of Neural Engineering, 20*(4), 046014. https://doi.org/10.1088/1741-2552/ace4f4

Lee, J., & Kim, H.-J. (2022). Normal Aging Induces Changes in the Brain and Neurodegeneration Progress: Review of the Structural, Biochemical, Metabolic, Cellular, and Molecular Changes. *Frontiers in Aging Neuroscience, 14*, 931536. https://doi.org/10.3389/fnagi.2022.931536

Miranda, P. C., Lomarev, M., & Hallett, M. (2006). Modeling the current distribution during transcranial direct current stimulation. *Clinical Neurophysiology, 117*(7), 1623–1629. https://doi.org/10.1016/j.clinph.2006.04.009

Opitz, A., Paulus, W., Will, S., Antunes, A., & Thielscher, A. (2015). Determinants of the electric field during transcranial direct current stimulation. *NeuroImage, 109*, 140–150. https://doi.org/10.1016/j.neuroimage.2015.01.033

Puonti, O., Van Leemput, K., Saturnino, G. B., Siebner, H. R., Madsen, K. H., & Thielscher, A. (2020). Accurate and robust whole-head segmentation from magnetic resonance images for individualized head modeling. *NeuroImage, 219*, 117044. https://doi.org/10.1016/j.neuroimage.2020.117044

Saturnino, G. B., Puonti, O., Nielsen, J. D., Antonenko, D., Madsen, K. H., & Thielscher, A. (2019). SimNIBS 2.1: A Comprehensive Pipeline for Individualized Electric Field Modelling for Transcranial Brain Stimulation. In S. Makarov (Eds.) et. al., *Brain and Human Body Modeling: Computational Human Modeling at EMBC 2018*. (pp. 3–25). Springer.

Shahid, S., Wen, P., & Ahfock, T. (2011). Effect of fat and muscle tissue conductivity on cortical currents—A tDCS study. *The 2011 IEEE/ICME International Conference on Complex Medical Engineering,* 211–215. https://doi.org/10.1109/ICCME.2011.5876735

Stolte, S. E., Indahlastari, A., Chen, J., Albizu, A., Dunn, A., Pedersen, S., See, K. B., Woods, A. J., & Fang, R. (2024). Precise and Rapid Whole-Head Segmentation from Magnetic Resonance Images of Older Adults Using Deep Learning. *Imaging Neuroscience, 2*. https://doi.org/10.1162/imag_a_00090

Thair, H., Holloway, A. L., Newport, R., & Smith, A. D. (2017). Transcranial Direct Current Stimulation (tDCS): A Beginner's Guide for Design and Implementation. *Frontiers in Neuroscience, 11*, 641. https://doi.org/10.3389/fnins.2017.00641

The MathWorks Inc. (2022). MATLAB version: 9.13.0 (R2022b), Natick, Massachusetts: The MathWorks Inc. https://www.mathworks.com

Vergallito, A., Varoli, E., Pisoni, A., Mattavelli, G., Del Mauro, L., Feroldi, S., Vallar, G., & Romero Lauro, L. J. (2023). State-dependent effectiveness of cathodal transcranial direct current stimulation on cortical excitability. *NeuroImage, 277*, 120242. https://doi.org/10.1016/j.neuroimage.2023.120242